Metallomics

Accepted Manuscript

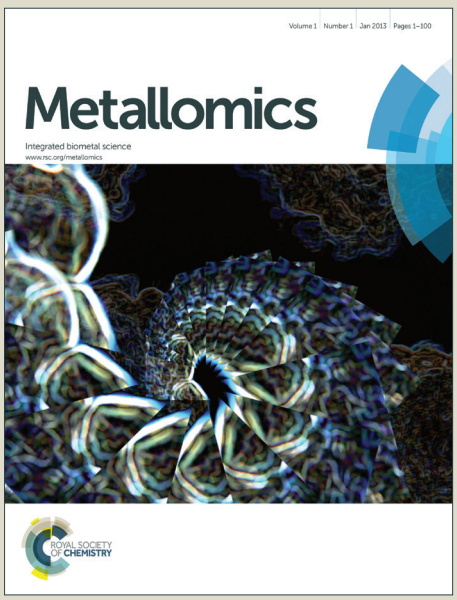

ROYAL SOCIETY OF CHEMISTRY

www.rsc.org/metallomics

Small angle X-ray scattering analysis of Cu^{2+}-induced oligomers of the Alzheimer's amyloid β peptide.

Timothy M. Ryan[1*], Nigel Kirby[2], Haydyn D.T. Mertens[2,3], Blaine Roberts[1,], Kevin J. Barnham[1,4], Roberto Cappai[4], Chi Le Lan Pham[3,5], Colin L. Masters[1] and Cyril C. Curtain[1,4]

[1]*University of Melbourne, Florey Institute of Neuroscience and Mental Health, Victoria 3010, Australia*

[2] *SAXS/WAX Beamline, The Australian Synchrotron, 800 Blackburn Road Clayton, Victoria 3168, Australia*

[3] *Present address Biological Small Angle Scattering Group European Molecular Biology Laboratory c/o DESY Notkestrasse 85, Geb. 25a22603 Hamburg, Germany*

[4]*Department of Pathology, Bio21 Molecular Science and Technology Institute, The University of Melbourne Victoria, 3010, Australia*

[5]*Present address School of Molecular Bioscience, DO6 Blackburn Building, The University of Sydney NSW 2006 Australia*

***** *Corresponding author**;** Dr T. M. Ryan, Florey Institute of Neuroscience and Mental Health, Level 4, Kenneth Myer Building at Genetics Lane on Royal Parade Parkville, Vic 3010 tmryan@unimelb.edu.au, Ph: +61390356728*

Abstract

Research into causes of Alzheimer's disease and its treatment has produced tantalising array of hypotheses about the role of transition metal dyshomeostasis, many of them on the interaction of these metals with the neurotoxic amyloid-β peptide (Aβ). Here, we have used small angle X-ray scattering (SAXS) to study the effect of the molar ratio, Cu^{2+}/ Aβ, on the early three-dimensional structures of the $A\beta_{1-40}$ and Cu^{2+}/ $A\beta_{1-42}$ peptides in solution. We found that at molar ratios of 0.5 copper to peptide $A\beta_{1-40}$ aggregated, while $A\beta_{1-42}$ adopted a relatively monodisperse cylindrical shape, and at a ratio of 1.5 copper to peptide $A\beta_{1-40}$ adopted a monodisperse cylindrical shape, while $A\beta_{1-42}$ adopted the shape of an ellipsoid of rotation. We also found, via in-line rapid mixing SAXS analysis, that both peptides in the absence of copper were monodisperse at very short timeframes (<2 sec). Kratky plots of these scattering profiles indicated that immediately after mixing both were intrinsically disordered. Ensemble optimisation modelling reflected this, indicating a wide range of structural conformers. These data reflect the ensembles from which the Cu^{2+}-promoted oligomers were derived. Our results are discussed in the light of other studies that have shown that the Cu^{2+}/ Aβ has a marked effect on fibril and oligomer formation by this peptide, with a higher ratio favouring the formation of cytotoxic non-amyloid oligomers. Our results are relatively consistent with previous two-dimensional studies of the conformations of these Cu^{2+}- induced entities, made on a much longer time-scale than SAXS, by transmission electron microscopy and atomic force microscopy, which showed that a range of oligomeric species are formed. We propose that SAXS carried out on a modern synchrotron beamline enables studies on initial events in disordered protein folding on physiologically-relevant time-scales,

and will likely provide great insight into the initiating processes of the Aβ misfolding, oligomerisation and amyloid formation.

Introduction:

Progressive neurodegeneration associated with deposits of aggregated amyloid β peptide (Aβ) in plaques in the brain is the hallmark of Alzheimer's disease (AD). The condition, which poses a major public health burden in all aging populations, is characterised by an individually variable decline in cognitive function and selective neuronal atrophy accompanied by loss of cortical volume in areas involved in learning and memory. While there is a weak correlation between plaque load in the brains of human subjects and animal models and the rate of cognitive impairment,[1] mounting evidence suggests that amyloid fibrils themselves are non-toxic end-products,[2] which may represent an equilibrium sink for toxic intermediates. Consequently, there has been increasing interest in soluble oligomers of Aβ that seem to be particularly toxic[3-7]. Unfortunately, synthetic Aβ is very responsive to *in vitro* environmental conditions. Accordingly, very large ranges of toxic oligomeric preparations have been reported, including amyloid derived, diffusible ligands (ADDLS), globulomers and amylospheroids (for review see Teplow *et al*[8]) This wide range of species has complicated the elucidation of their significance in AD pathogenesis[9].

One factor that significantly influences Aß aggregation is the presence of ions of transition metals, particularly copper and zinc. These ions can significantly affect the formation of both oligomers and amyloid fibrils *in vitro*. In addition, there is some evidence that metal dyshomeostasis in the ageing brain may contribute to the

development of AD, with extra-cellular copper pools being regarded as a potentially critical factor in the development of the disease[10].

Some studies have shown Cu^{2+} at sub-equimolar metal ion/peptide ratios can induce the aggregation of $A\beta_{1-42}$ into Thioflavin T (ThT) positive fibrils, while at supra-equimolar ratios non-fibrillar oligomers are formed that have been shown to be toxic to neuronal cells in culture[11-13]. Other studies have found that both sub and supra-molecular Cu^{2+}/peptide led to the ThT-negative species, implying the absence of cross-β-sheet structures[14, 15]. This dichotomy is intriguing, and may have its basis in the method of preparation of Aβ, which can vary significantly, and can result in dramatically different biophysical properties of the peptide (for example see Ryan *et al.*[16]).

However, little is known about the structural differences between the oligomers and fibrils that might account for these differences in toxicity. Transmission electron microscopy showed $A\beta_{1-42}$ in the presence of 1:1 Mole/Mole (M/M) or greater Cu^{2+} forms spheres approximately 10-20 nm in size, while at <1:1 M/M fibrils were observed [11]. In another study using transmission electron microscopy and atomic force microscopy granular structures were found with $A\beta_{1-42}$ in the presence of supra-equimolar Cu^{2+} [12], while at supra-equimolar Cu^{2+} $A\beta_{1-40}$ formed thin ribbon-like structures that resemble amyloid fibres[12, 17]. The molecular basis for these alternate morphologies is elusive, and warrants further investigation to determine the basis for the disparate toxicity levels.

Small-angle X-ray scattering (SAXS) is a widely used low-resolution technique for structural characterisation of proteins in solution[18]. Recent developments in *ab initio* modelling based on the data extracted from the scattering profiles enable the quantitative characterisation of the in solution structures of very large protein

assemblages, which either fail to crystallise, and hence cannot be investigated by X-ray crystallography, are relatively short lived or are too large to be analysed by solution state NMR. Solid-state NMR can achieve relatively high-resolution measures; however this technique only gives a representation of the final aggregated (and hence solid) conformation. Here, we describe a SAXS study of the earliest $A\beta_{1-40}$ and $A\beta_{1-42}$ structures formed in the presence of sub- and supra-equimolar ratios of Cu^{2+}.

Materials and methods

Aß preparation.

Dry Synthetic $A\beta_{1-40}$ and $A\beta_{1-42}$ (Keck laboratories, Yale) were weighed and dissolved in hexafluro-2-isopropanol (HFIP) and incubated at 25°C for 1 h to remove any preformed aggregates. The peptides were then aliquotted into equal amounts and dried by using a speed-vac. Before use, aliquots were dissolved in 15 mM NaOH, sonicated in a water bath containing ice for 15 min and centrifuged in a bench-top centrifuge at 16,000 x *g* for 20 min. The final peptide concentration was 3.75 mg/mL (as determined spectrophotmetrically, with 214nm absorbance and extinction coefficients of 95426 mol^{-1} cm^{-1} and 91264 mol^{-1} cm^{-1} for $Aß_{1-42}$ and $Aß_{1-40}$). This was diluted fivefold with a buffer consisting of 10 mM sodium phosphate, 150 mM NaCl at pH 7.4, followed by sonication with a probe at 0.5 s intervals for 1 min at 30% power. The solution was then centrifuged in a benchtop centrifuge at 13,000 rpm for 20 min.

Previously, we have observed that $A\beta_{1-42}$ peptides in the absence of copper aggregate relatively rapidly, resulting in a solution that is polydisperse, and hence not appropriate for SAXS measurements. Thus, a custom, in-line rapid mixing device was developed to monitor Aβ refolding directly after buffer neutralisation. Scattering

measurements of the two forms of Aβ rapidly mixed from 15 mM KOH into the 10 mM phosphate 150 mM NaCl pH 7.4 buffer (i.e. without Cu^{2+}) were made with a custom built flow mixing apparatus. This consisted of a stainless steel 0.8 mm internal diameter "Y" shaped mixing piece connected to two microsyringes; one syringe delivering 100 μL of buffer and the sample syringe 10 μL of protein in KOH. The 1.5 mm quartz capillary located in the SAXS beam was joined to the outlet of the mixing piece by a 15 cm length of 0.8 mm internal diameter silicone tubing. Prior to the SAXS measurements, the efficiency of mixing was determined by measuring photometrically the distribution in the capillary of dye injected into the system at different flow rates. However because of concerns regarding reaction of the Cu^{2+} with the steel tubing and syringe plungers introducing Fe ions into the system[19] the apparatus was not used in the experiments where Cu^{2+} was added to the peptides. Trace Fe ions in combination with Cu^{2+} can set up a Fenton redox cycle that could lead to oxidative damage to the peptides, even within the short time-scale of our experiment[20].

Here, 25 mM Cu^{2+} was prepared as 1 part $CuCl_2$ to 6 parts glycine (Gly) in H_2O. The addition of a glycine counter-ion was essential to prevent the formation of insoluble phosphate Cu complexes. Because of the known tendency of $A\beta_{1-40}$ and $A\beta_{1-42}$ to show signs of aggregation in the presence of Cu^{2+} within times as short as 30 min.[19], the $CuCl_2$/Gly was added to the reaction mixture at the required concentration from the 25 mM stock solution immediately before the SAXS measurements. Buffer equilibration was performed on a PD-10 desalting column (GE Healthcare) equilibrated with the $CuCl_2$/Gly 10 mM sodium phosphate 150 mM NaCl pH 7.4 buffer, resulting in a final concentration of 100 μM of protein. Samples were centrifuged at 16,000 x *g* for 10 minutes and immediately introduced into the SAXS

beamline. The whole process took place within 20 min. Protein concentration of an aliquot of each sample was determined by using the extinction coefficient at 214nm of 95,426 M^{-1} cm^{-1} and 91,264 M^{-1} cm^{-1} for $A\beta_{1-42}$ and $A\beta_{1-40}$, respectively.

S*mall- angle X-ray scattering (SAXS) measurements*

Measurements were made using the high-intensity undulator source on the SAXS/WAXS beamline of the Australian Synchrotron (Clayton, Victoria, Australia)[21]. An energy resolution of 10^{-4} was obtained from a cryo-cooled Si (III) double-crystal monochromator, and the beam size (fwhm focused at the sample) was 250 x 100 μm with a total photon current of approximately 2 x 10^{12} photons sec^{-1}. The maximum q range used was 0.005 to 0.35 $Å^{-1}$ (where $q = 4\pi \sin\theta/\lambda$, 2θ is the X-ray scattering angle and λ the X-ray wavelength, 1.03 Å). Absolute intensities were calibrated using water in the 1.5 mm ID quartz capillary. The samples were slowly pumped through 1.5 mm quartz capillaries (Hampton Research, Aliso Viejo, CA USA) and 25 exposures were made at 1.2 sec. intervals. The exchange buffer was used as the scattering blank.

Analysis of SAXS data

All patterns obtained were reduced to one-dimensional profiles of intensity I versus q using the Saxs15id software package[22]. Individual frame profiles were inspected to ensure that there were no outliers and that those from the initial exposures were identical to those from the last indicating absence of radiation damage or, in the cases of the proteins with added Cu^{2+}, changes in oligomerisation. Radius of gyration (R_g) calculation using AUTORG, Kratky plots (q vs $q^2I(q)$, Guinier (Ln $I(q)$ vs q^2) and Porod analyses and the determination of the size and shape of the molecules in solution from the SAXS profiles were made using the ATSAS suite of programs 2.5.0-2 release[23-26] available from http://www.embl-

Hamburg.de/ExternalInfo/Research/Sax/index.html. The data were processed and the overall parameters were computed following standard procedures using the program PRIMUS. Radii of gyration (Å) were calculated from both Guinier and pair distribution function, *P*(r), analysis. AUTOPOROD[27] and the MULCh server of The School of Molecular Biosciences, University of Sydney (http://smb-research.smb.usyd.edu.au)[28] were used to calculate estimated particle volume and molecular mass. Data were regularised by the indirect Fourier transformation method implemented in the program GNOM [29] and were used as input into DAMMIF [30] (online at www.embl-hamburg.de/biosaxs/atsas-online/dammif.php) to build *ab initio* models of the protein shapes by simulated annealing. DAMMIF was run 20 times on the same input data and the output models were aligned and averaged using DAMAVER. Molecular dimensions were estimated using HYPERCHEM® and final illustrations were prepared with RasMol 2.7.4.

Where scattering indicated a fully flexible protein, ensemble optimisation modelling (EOM) was employed[31]. This approach is based on the generation of a large pool (typically10,000) of theoretical structures derived with side-chain interaction constraints from the primary sequence of the protein. The theoretical X-ray scattering profiles calculated from these structures are then matched for fit using a genetic algorithm against the experimental scattering profile to create an ensemble of best fit structures. The parameters of these selected structural give a distribution for the best fits for R_g and D_{max}, which can be used to determine variations in flexibility and conformation.

Results

Rapid addition of $A\beta_{1\text{-}40\ and}$ $A\beta_{1\text{-}42}$ to non-Cu^{2+} containing buffer leads to rapid development of polydispersity

Studies of the initial conformation of

Aβ □□□□□□□□□□□□□□□□□□□□□□□□□□□□ are essential for understanding its interactions with metal ions, and in understanding the changes that these metal ions induce in its structure. Unfortunately, the high propensity of Aβ to aggregate at any appreciable concentration makes obtaining these data difficult. To investigate the earliest stages of Aβ refolding, we used the custom in-line rapid mixing device to acquire data at 1.2 second intervals for Aβ refolded into PBS buffer from 15mM KOH (Fig. 1 A & B), to a final concentration of 1mg/mL. Both $A\beta_{1-40}$ (Fig. 1A) and $A\beta_{1-42}$ (Fig. 1B) displayed rapid aggregation resulting in polydispersity 2.4-3.6 seconds after mixing. However, the data acquired for the first point at 1.2 seconds was monodisperse (as indicated by Guinier analysis[32], plot not shown), indicating a lack of aggregated material. MULCh analysis of the scattering data gave values of 5 ± 1 kD for both peptides, again indicating a relatively monomeric status upon initial refolding. Kratky analysis of both 1.2 second exposures (Fig 1 C & D) indicated that the proteins at this stage were highly flexible meaning that the scattering curve could encompass a wide range of possible conformations. Ensemble optimisation modelling showed such a wide distribution of conformers for both peptides (Panels E and F, G and H). As could be expected from inspection of profiles shown in Fig. 1A and Fig. 1B there is a significant difference between the conformer profiles of the two peptides. The ensemble Rg max values were 30.5 and 28.5 for the and respectively, compared with 20.5 for the random pool. This difference is an indication of a significant number of extended conformers in both ensembles. The D_{max} distribution for $A\beta_{1-42}$ (Fig. 1F) reflects a slightly greater proportion of extended compact conformers than the distribution for $A\beta_{1-40}$ (Fig.1H). Yang and Teplow[33] performed μsec time-scale replica exchange molecular dynamics simulations to sample the

conformational space of the $A\beta_{1-40}$ and $A\beta_{1-42}$ monomers and showed that neither peptide was completely unstructured, in agreement with our SAXS findings.

SAXS profiles of $A\beta_{1-40}$ mixed with sub and supra-equimolar Cu^{2+}

SAXS analysis of Aβ in the presence of copper resulted in a series of interesting results (Figure 2). $A\beta_{1-40}$ in the presence of sub-stoichiometric Cu^{2+} displayed an asymptotic increase at low angles (figure 2A, ii), indicative of aggregation, and a nonlinear Guinier region, which renders this data unanalysable (figure 2D, ii). For comparison curve iii shows the similar 4.8 sec. profile for $A\beta_{1-40}$ rapidly mixed from KOH solution into buffer. On the other hand, the profile of $A\beta_{1-40}$ in the presence of supra-stoichiometric Cu^{2+} indicated a relatively monodisperse solution (figure 2A, i). A Kratky plot of the supra-stoichiometric Cu^{2+} ratio indicated globular structure (Figure 2B), and the particle distance distribution function (*P(r)*) (Fig. 2C), in conjunction with Guinier analysis (Fig. 2D, i) suggested a monodisperse solution with an R_g and D_{max} of 39.7±1Å and 123±2Å, respectively Table 1). The closeness of the Guinier R_g and that obtained from the *P(r)* calculation (Table 1) also supported the suggestion of monodispersity[32]. Porod and MULCh analysis provided values of 47±3 kDa and 51±1kDa, respectively. These results indicate that $A\beta_{1-40}$ in supra-stoichiometric concentrations of copper forms a relatively stable large oligomer.

SAXS profiles of $A\beta_{1-42}$ equilibrated with sub and supra-equimolar Cu^{2+}

In contrast to $A\beta_{1-40}$, $A\beta_{1-42}$ is monodisperse in the presence of both supra (profile i) and sub (profile ii) stoichiometric concentrations of Cu^{2+} (Fig. 3A). However, the scattering data indicates that $A\beta_{1-42}$ has two very distinct conformations in the varying concentrations of Cu^{2+}. Kratky analysis indicates that these two profiles represent globular structures (Fig. 3B), while evaluation of the particle distance distribution function (*P(r)*) with GNOM (Fig.3C) and Guinier analysis (Fig. 3D) indicated that the

R_g's were 54.5 ± 1Å and 77 ± 1Å for the low and high Cu^{2+} ratios, respectively, while the values obtained from the *P(r)* calculation were, respectively, 125.5 ± 1Å and 185 ± 1Å (Table1). The Porod and MULCh analysis indicate molecular weights of 96 ± 3 kDa and 98 ± 1kDa for low Cu^{2+}, respectively, while for high Cu^{2+} values of 158 ± 4 kDa and 161 ± 4kDa, respectively, were obtained. These results strongly suggest that $A\beta_{1-42}$ forms large oligomers of differing conformation on the basis of the stoichiometric ratio of Cu^{2+}.

Ab initio modelling of the high Cu^{2+}/peptide $A\beta_{1-40}$ and high and low $A\beta_{1-42}$ complexes

The D_{max} values indicate that $A\beta_{1-40}$ in the presence of high Cu^{2+} and the $A\beta_{1-42}$ Cu^{2+} samples were relatively elongated. In a fitting procedure using the ATSAS program BODIES, the scattering profiles of the complexes were approximated by those generated from simple homogenous geometrical bodies (Figure 4). Using this approach the 1.5 M/M $Cu^{2+}/A\beta_{1-40}$ could not be suitably described (with discrepancy, $\chi > 2.0$) by any of the cylinder, ellipsoid, sphere or dumb-bell bodies (curve i is an attempt at cylinder fit), while that of the 0.5 M/M $Cu^{2+}/A\beta_{1-42}$ (ii) was very well represented by a cylinder of length 193 Å and diameter 37 Å ($\chi = 0.85$). Similarly, the1.5 M/M $Cu^{2+}/A\beta_{1-42}$ data (iii) were reasonably fit by an ellipsoid of rotation with diameter 110 Å and max depth 68 Å ($\chi = 1.6$). Nevertheless, we must bear in mind two-dimensional scattering data can give several possible three-dimensional structures and the failure of the simple BODIES fitting procedure in the case 1.5 M/M $Cu^{2+}/A\beta_{1-40}$ illustrates that this procedure is not necessarily infallible.

In another approach, *ab initio* models were reconstructed from the experimental scattering data for each of the three monodisperse samples using the bead modelling program DAMMIF[34]. Clustering analysis based upon the normalised spatial

discrepancies between input models was conducted to assess the similarity of the reconstructions, where the closer the distance between two pairs of models the more closely they resemble each other. The small relative distances between clusters are given in Table 2 indicate that the *ab initio* reconstructions for each sample are robust. It is likely that the poor fit of the 1.5 M/M $Cu^{2+}/A\beta_{1-40}$ profile by any of the BODIES shapes was due to the noise at its higher *q* values. Bead modelling is less sensitive to this region. The shapes of the bead models produced were essentially extended and rod-like for both 1.5 M/M $Cu^{2+}/A\beta_{1-40}$ and 0.5 M/M $Cu^{2+}/A\beta_{1-42}$ samples, but compact and discoidal for 1.5 M/M $Cu^{2+}/A\beta_{1-42}$. This was consistent with the Kratky plots suggesting that the complexes were relatively globular and likely folded. Although the depicted shapes are reasonable solutions for modelling from the mathematical point of view, it is desirable to seek confirmation from independent data, which are usually crystallographic or NMR derived models of the oligomer subunits. Monomeric Aβ in solution, however, is intrinsically unstructured, molecular dynamics simulation showing it to populate a range of conformations[35, 36]. This is confirmed in our EOM analysis of the scattering data from the rapid mixing experiment where at physiological pH and ionic strength both peptides rapidly assumed an unstructured conformation before aggregating. However, the Kratky plots generated from the SAXS data of the Cu^{2+} complexes are consistent with folded peptide in each case, indicating that the binding of Cu^{2+} leads to structural stabilisation. Dividing the molecular mass of the 1.5 M/M $Cu^{2+}/A\beta_{1-42}$ by the molecular mass of $A\beta_{1-42}$ suggests that it consists of 38 peptide monomers, while the elongated 1.5 M/M $Cu^{2+}/A\beta_{1-40}$ and 0.5 M/M $Cu^{2+}/A\beta_{1-42}$ consist of 10 and 20 peptides, respectively. The length of an extended β strand conformation of $A\beta_{1-42}$ is 118 Å while that for $A\beta_{1-40}$ is 115 Å. Since the conformations of the complexes are

dependent on the Cu^{2+}/peptide ratio, we would expect the known Cu^{2+} coordination sites, at the N-terminal end of the peptides, to be involved in their formation[37-40]. At the C-terminal half of the peptide there are the two zipper sequences; the Gly-XXX-Gly-XXX-Gly motif that has been proposed to mediate the formation of toxic oligomers[41] and the C-terminal sequence starting at M35[42]. In both kinds of zipper M35 plays a prominent role. Solid-state NMR experiments [43] have demonstrated that dimerization of protofibrils involves the formation of an inter-sheet steric zipper via M35–M35 for both $A\beta_{1-40}$ and $A\beta_{1-42}$. However, participation of M35 presents an important constraint on the role of both kinds of zipper in the formation of the Cu^{2+} induced oligomers/protofibrils. It has been shown that $A\beta_{1-42}$ fibrils formed in the presence of Zn^{2+} are resistant to matrix metalloprotease 2, which cleaves Aβ at L34-M35, while fibrils and protofibrils formed in the presence of 0.1-10 M/M Cu^{2+} are degraded [44]. This finding suggests that the oligomers/protofibrils formed in the presence of Cu^{2+} must be either sufficiently loosely packed to allow access of the protease or are in equilibrium with monomeric species. A possible packing arrangement for the 1.5 M/M $Cu^{2+}/A\beta_{1-42}$ is shown in the cartoon in Figure 5 where 19 peptides can be fitted into each half of an ellipsoid of rotation of the dimensions indicated by the scattering data. The overlap necessary to fit into the depth of the ellipsoid covers the two above-mentioned zipper regions.

Discussion:

The Aβ peptides are cleaved from the amyloid-β protein precursor (APP) by the two proteases, β-and γ-secretase. Studies in transgenic mice and cell and hippocampal slice cultures show that Aβ oligomers modulate both pre- and postsynaptic structures and functions in a dose- and assembly-dependent manner. A major task for the study of the biophysics of Aβ peptides is to relate *in vitro* observations of their modes of

assembly to what is known of their *in vivo* behaviour. However, establishing this relationship is difficult as the *in vitro* and *in vivo* spheres of action have contrasting time-scales. On release from the APP into the synaptic cleft the peptides are confronted with a *milieu* containing Zn and Cu ions and membrane surfaces within a small space that would be conducive to rapid reactions. SAXS performed on a synchrotron beamline can generate data on a time-scale of seconds. It, therefore, is a good method for studying the collapse of inherently disordered proteins into more compact conformers that could be the basis of larger assemblages. NMR studies[45, 46] have been carried out on fibrillar structures in the presence of Cu, using magic angle spinning, and on Aβ in structure promoting environments[47], while ion mobility coupled with mass spectrometry has been used to characterise different oligomer states of $A\beta_{1\text{-}40}$ and $A\beta_{1\text{-}42}$ in the absence of Cu[48]. They have made a very significant contribution to our understanding of the structural relationships between the peptides forming amyloids, but typically provide information on events that occur late in the aggregation pathway.

Our findings on the effect of Cu^{2+} on Aβ folding agree broadly with what is already known of the effect of Cu^{2+} concentration on the polymerisation of Aβ. Smith *et al.*[11] found that at sub-equimolar Cu^{2+}/peptide molar ratios $A\beta_{1\text{-}42}$ formed thioflavin-T reactive non toxic fibrils, however at supra-equimolar Cu^{2+} /peptide molar ratios it formed toxic oligomers. Transmission electron microscopy showed these to be approximately 10-20 nm in diameter and associated with large amorphous aggregates. Jin *et al.*[12] found that the only significant effect on $A\beta_{1\text{-}40}$ of equimolar Cu^{2+}/peptide was to produce thin (proto) fibrils as observed by TEM and AFM. However $A\beta_{1\text{-}42}$ showed increased aggregation in the presence of Cu^{2+}, which induced granular aggregates and enhanced $A\beta_{1\text{-}42}$'s cytotoxicity. The structure obtained in our SAXS

studies of the supra-equimolar $Cu^{2+}/A\beta_{1-42}$ was somewhat smaller in diameter (Fig. 5C) and consistent with a monodisperse solution of oligomeric discoidal/ellipsoidal particles. It is highly likely that these differences are also due to differences in the initial aggregation propensity of the different batches of peptide and the method used for their initial solubilisation. Significantly, the 7 nm thickness of the ellipsoid of rotation is compatible with the estimate of 20 nm for the width of the synaptic cleft [49] which is one of the likely sites of Aβ oligomer toxicity[50].

Smith *et al.*[11] showed the presence of dityrosine in the supra-molecular $Cu^{2+}/A\beta_{1-42}$ oligomers. Cu^{2+} induced formation of di-tyrosine may be a mechanistic cause of the increase in Aβ cytotoxicity observed upon treatment with Cu^{2+} [11]. Barnham *et al.*[51] showed that Cu-facilitated redox processes involving tyrosine at position 10 of Aβ could produce reactive oxygen species contributing to the cytotoxicity of Aβ peptides in the presence of Cu^{2+}. A feature of this reaction was that it required Cu-Cu distances of approximately 6Å, as shown by EPR studies showing dipolar interaction effects in the spectra of supra-equimolar $Cu^{2+}/A\beta_{1-42}$ that were not observed with sub-equimolar preparations[52]. It is, therefore, possible that the compact structure of the discoidal oligomers formed in the presence of supra-equimolecular Cu^{2+} concentrations demonstrated by our SAXS study would facilitate Cu-Cu interaction and hence toxicity, while the more extended structures found at a lower Cu^{2+} concentration may not facilitate this arrangement. Alternatively, toxicity may be increased by enhancement of cross-linking of synaptic membrane receptors by the Aβ N-terminal regions in the discoidal structure. Cross-linking leading to synaptotoxicity has been suggested as an Aβ toxicity mechanism[53].

Conclusion:

We show that sub-equimolecular concentrations of copper ions induce the formation of elongated Aβ structures consistent with protofibrils, while supra-equimolecular concentrations of copper ions induce $A\beta_{1-42}$ to form ellipsoidal oligomers, consistent with postulated toxic oligomeric species that have been observed microscopically. The SAXS results show that these structures form rapidly, and are relatively well ordered, suggesting that they are likely to interact specifically with larger macromolecular structures. In addition, our results show the utility of SAXS in understanding the complex behaviour observed in aggregation prone systems, and the potential insight that can be gained through rapid analysis of protein folding and self-association.

Acknowledgements:

The authors wish to acknowledge the support of the Australian Synchrotron and the Victorian Government Operational Infrastructure Support Program. TMR is supported by the Australian Alzheimer's disease foundation. CLM and KJB are consultants for Prana Biotechnology Pty ltd. CLM, KJB and RC are the principal investigators on an NHMRC program grant

References

1. Lim YY, Ellis KA, Harrington K, Kamer A, Pietrzak RH, Bush AI, Darby D, Martins RN, Masters CL, Rowe CC, Savage G, Szoeke C, Villemagne VL, Ames D and M. P., *Neuropsychology*, 2013, **27**, 322-332.
2. M. E. Larson and S. E. Lesne, *J Neurochem*, 2012, **120 Suppl 1**, 125-139.
3. S. Lesne and L. Kotilinek, *J Neurosci*, 2005, **25**, 9319-9320.
4. S. Lesne, L. Kotilinek and K. H. Ashe, *Neuroscience*, 2008, **151**, 745-749.
5. G. M. Shankar, B. L. Bloodgood, M. Townsend, D. M. Walsh, D. J. Selkoe and B. L. Sabatini, *J Neurosci*, 2007, **27**, 2866-2875.
6. G. M. Shankar, S. Li, T. H. Mehta, A. Garcia-Munoz, N. E. Shepardson, I. Smith, F. M. Brett, M. A. Farrell, M. J. Rowan, C. A. Lemere, C. M. Regan, D. M. Walsh, B. L. Sabatini and D. J. Selkoe, *Nat Med*, 2008, **14**, 837-842.
7. G. M. Shankar, A. T. Welzel, J. M. McDonald, D. J. Selkoe and D. M. Walsh, *Methods Mol Biol*, 2011, **670**, 33-44.
8. D. B. Teplow, *Alzheimer's research & therapy*, 2013, **5**, 39.
9. I. Benilova, E. Karran and B. De Strooper, *Nat Neurosci*, 2012, **15**, 349-357.
10. A. I. Bush, *J Alzheimers Dis*, 2012.

11. D. P. Smith, G. D. Ciccotosto, D. J. Tew, M. T. Fodero-Tavoletti, T. Johanssen, C. L. Masters, K. J. Barnham and R. Cappai, *Biochemistry*, 2007, **46**, 2881-2891.
12. L. Jin, W. H. Wu, Q. Y. Li, Y. F. Zhao and Y. M. Li, *Nanoscale*, 2011, **3**, 4746-4751.
13. J. T. Pedersen, J. Ostergaard, N. Rozlosnik, B. Gammelgaard and N. H. Heegaard, *J Biol Chem*, 2011, **286**, 26952-26963.
14. X. H. Yang, H. C. Huang, L. Chen, W. Xu and Z. F. Jiang, *J Alzheimers Dis*, 2009, **18**, 799-810.
15. M. Mold, L. Ouro-Gnao, B. M. Wieckowski and C. Exley, *Scientific reports*, 2013, **3**, 1256.
16. T. M. Ryan, J. Caine, H. D. Mertens, N. Kirby, J. Nigro, K. Breheney, L. J. Waddington, V. A. Streltsov, C. Curtain, C. L. Masters and B. R. Roberts, *PeerJ*, 2013, **1**, e73.
17. S. Jun and S. Saxena, *Angew Chem Int Ed Engl*, 2007, **46**, 3959-3961.
18. H. D. Mertens and D. I. Svergun, *J Struct Biol*, 2010, **172**, 128-141.
19. C. S. Atwood, R. D. Moir, X. Huang, R. C. Scarpa, N. M. Bacarra, D. M. Romano, M. A. Hartshorn, R. E. Tanzi and A. I. Bush, *J Biol Chem*, 1998, **273**, 12817-12826.
20. M. Brzyska, A. Bacia and D. Elbaum, *European journal of biochemistry / FEBS*, 2001, **268**, 3443-3454.
21. N. M. Kirby, S. T. Mudie, A. M. Hawley, D. J. Cookson, H. D. Mertens, N. Cowieson and V. Samardzic-Boban, *Journal of Applied Crystallography*, 2013, **46**, 1670-1680.
22. D. Cookson, N. Kirby, R. Knott, M. Lee and D. Schultz, *Journal of synchrotron radiation*, 2006, **13**, 440-444.
23. P. V. Konarev, M. V. Petoukhov, V. V. V olkov and D. I. Svergun, *J Appl Crystallography*, 2006, **39**, 277-286.
24. P. V. Konarev, V. V. Volkov, A. V. Sokolova, K. M.H.J. and D. I. Svergun, *J Appl Crystallography* 2003, **36**, 1277-1282.
25. P. V. Konarev, M. V. Petoukhov and D. I. Svergun, *J Appl Crystallography*, 2001, **34**, 527-532.
26. D. I. Svergun, *Biophys J*, 1999, **76**, 2879-2886.
27. M. V. Petoukhov and D. I. Svergun, *The international journal of biochemistry & cell biology*, 2013, **45**, 429-437.
28. A. E. Whitten, S. Cai and J. Trewhella, *J Appl Cryst*, 2008, **41**, 222-226.
29. D. I. Svergun, *J. Appl. Crystallogr.* , 1992, **25**, 495-503.
30. M. V. Petoukhov, D. Franke, A. V. Shkumatov, G. Tria, A. G. Kikhney, M. Gajda, C. Gorba, H. D. T. Mertens, P. V. Konarev and D. I. Svergun, *Journal of Applied Crystallography*, 2012, **45**, 342-350.
31. P. Bernado and D. I. Svergun, *Mol Biosyst*, 2012, **8**, 151-167.
32. D. A. Jaques and J. Trewhella, *Protein Science*, 2010, **19**, 642-657.
33. M. Yang and D. B. Teplow, *Journal of molecular biology*, 2008, **384**, 450-464.
34. D. Franke and D. I. Svergun, *J. Appl. Crystallogr.*, 2009, **42**, 342-346.
35. J. Ikebe, N. Kamiya, J. Ito, H. Shindo and J. Higo, *Protein Sci*, 2007, **16**, 1596-1608.
36. J. P. Colletier, A. Laganowsky, M. Landau, M. Zhao, A. B. Soriaga, L. Goldschmidt, D. Flot, D. Cascio, M. R. Sawaya and D. Eisenberg, *Proc Natl Acad Sci U S A*, 2011, **108**, 16938-16943.

37. S. C. Drew and K. J. Barnham, *Acc Chem Res*, 2011, **44**, 1146-1155.
38. S. C. Drew, C. L. Masters and K. J. Barnham, *J Am Chem Soc*, 2009, **131**, 8760-8761.
39. S. C. Drew, C. L. Masters and K. J. Barnham, *PLoS One*, 2010, **5**, e15875.
40. S. C. Drew, C. J. Noble, C. L. Masters, G. R. Hanson and K. J. Barnham, *J Am Chem Soc*, 2009, **131**, 1195-1207.
41. V. Fonte, V. Dostal, C. M. Roberts, P. Gonzales, P. Lacor, J. Magrane, N. Dingwell, E. Y. Fan, M. A. Silverman, G. H. Stein and C. D. Link, *Mol Neurodegener*, 2011, **6**, 61.
42. R. Nelson, M. R. Sawaya, M. Balbirnie, A. O. Madsen, C. Riekel, R. Grothe and D. Eisenberg, *Nature*, 2005, **435**, 773-778.
43. T. Sato, P. Kienlen-Campard, M. Ahmed, W. Liu, H. Li, J. I. Elliott, S. Aimoto, S. N. Constantinescu, J. N. Octave and S. O. Smith, *Biochemistry*, 2006, **45**, 5503-5516.
44. P. J. Crouch, D. J. Tew, T. Du, D. N. Nguyen, A. Caragounis, G. Filiz, R. E. Blake, I. A. Trounce, C. P. Soon, K. Laughton, K. A. Perez, Q. X. Li, R. A. Cherny, C. L. Masters, K. J. Barnham and A. R. White, *J Neurochem*, 2009, **108**, 1198-1207.
45. S. Parthasarathy, F. Long, Y. Miller, Y. Xiao, D. McElheny, K. Thurber, B. Ma, R. Nussinov and Y. Ishii, *J Am Chem Soc*, 2011, **133**, 3390-3400.
46. S. Parthasarathy, B. Yoo, D. McElheny, W. Tay and Y. Ishii, *J Biol Chem*, 2014, **289**, 9998-10010.
47. J. D. Gehman, C. C. O'Brien, F. Shabanpoor, J. D. Wade and F. Separovic, *European biophysics journal : EBJ*, 2008, **37**, 333-344.
48. S. L. Bernstein, N. F. Dupuis, N. D. Lazo, T. Wyttenbach, M. M. Condron, G. Bitan, D. B. Teplow, J. E. Shea, B. T. Ruotolo, C. V. Robinson and M. T. Bowers, *Nat Chem*, 2009, **1**, 326-331.
49. B. Zuber, I. Nikonenko, P. Klauser, D. Muller and J. Dubochet, *PNAS*, 2005, **102**, 19192-19197.
50. H. Kokubo, R. Kayed, C. G. Glabe and H. Yamaguchi, *Brain Res*, 2005, **1031**, 222-228.
51. K. J. Barnham, F. Haeffner, G. D. Ciccotosto, C. C. Curtain, D. Tew, C. Mavros, K. Beyreuther, D. Carrington, C. L. Masters, R. A. Cherny, R. Cappai and A. I. Bush, *FASEB J*, 2004, **18**, 1427-1429.
52. C. C. Curtain, F. Ali, I. Volitakis, R. A. Cherny, R. S. Norton, K. Beyreuther, C. J. Barrow, C. L. Masters, A. I. Bush and K. J. Barnham, *J Biol Chem*, 2001, **276**, 20466-20473.
53. C. Bate and A. Williams, *J Biol Chem*, 2011, **286**, 37955-37963.

Figure legends:

Figure 1: Scattering data from rapid mix experiments. A) Profiles of $A\beta_{1-40}$ taken at 1.2 second intervals reading up from lowest curve after mixing from 15 mM KOH solution into 10 mM phosphate 150 mM NaCl pH 7.4 buffer. B) Profiles of $A\beta_{1-42}$ taken after mixing, 1.2 sec. intervals between curves also reading up from lowest

curve, C) Kratky plot calculated from the 1st 1.2 sec. $A\beta_{1-40}$ profile. D) Kratky plot from the 1.2 sec. $A\beta_{1-42}$ profile. E) R_g distribution calculated using Advanced EOM 2.0 from the 1.2 sec $A\beta_{1-42}$ profile. F) EOM derived D_{max} distribution for the 1.2 sec $A\beta_{1-42}$ profile. G) EOM derived R_g distribution for the 1.2 sec $A\beta_{1-40}$ profile. H) EOM derived D_{max} distribution for the 1.2 sec $A\beta_{1-40}$ profile. Dotted lines in panels E, F, G and H represent the pools of R_g and D_{max} values generated from the peptide sequences. The solid lines represent the ensemble values.

Figure 2: Scattering data for $Cu^{2+}/A\beta_{1-40}$ at sub and supra-equimolecular ratios. A) Scattering profiles. Curve (i) $A\beta_{1-40}$ in 1.5 M/M Cu^{2+}, (ii) $A\beta_{1-40}$ 0.5 M/M Cu^{2+} B) Kratky plot of 1.5 M/M $Cu^{2+}/A\beta_{1-40}$. C) Pair distribution analysis plot (P(r)) of 1.5 M/M $Cu^{2+}/A\beta_{1-40}$. D) Guinier plots of (i) 1.5 M/M $Cu^{2+}/A\beta_{1-40}$, (ii) 0.5M/M $Cu^{2+}/A\beta_{1-40}$, and (iii) $A\beta_{1-40}$ rapidly mixed from KOH to buffer.

Figure 3: Scattering data for $Cu^{2+}/A\beta_{1-42}$ in sub and supra-equimolecular ratios. A) Scattering profiles for (i) $A\beta_{1-42}$ in 1.5 M/M Cu^{2+}, (ii) $A\beta_{1-42}$ in 0.5 M/M Cu^{2+} and (iii) $A\beta_{1-42}$ in buffer for comparison. B) Kratky plots of (i) 1.5 M/M $Cu^{2+}/A\beta_{1-42}$, (ii) 0.5 M/M $Cu^{2+}/A\beta_{1-42}$. C) Pair distribution analysis plot (P(r)) of (i) 1.5 M/M $Cu^{2+}/A\beta_{1-42}$, (ii) 0.5 M/M $Cu^{2+}/A\beta_{1-42}$. D) Guinier plot of (i) 1.5 M/M $Cu^{2+}/A\beta_{1-42}$, (ii) 0.5 M/M $Cu^{2+}/A\beta_{1-42}$

Figure 4: Fit of cylindrical and ellipsoidal bodies to scattering profiles; (i) Lack of fit of a cylinder to 1.5 M/M $Cu^{2+}/A\beta_{1-42}$; (ii) Fit of a cylinder to the profile of 0.5 M/M $Cu^{2+}/A\beta_{1-42}$; (iii) Fit of an ellipsoid of rotation to the profile of 1.5 M/M $Cu^{2+}/A\beta_{1-42}$.

Figure 5: Cartoons of *ab initio* models produced by using DAMMIF of A. 1.5 M/M $Cu^{2+}/A\beta_{1-40}$, B. 0.5 M/M $Cu^{2+}/A\beta_{1-42}$, C. 1.5 M/M $Cu^{2+}/A\beta_{1-42}$, D. side view of ellipsoid of rotation, E and F showing how $A\beta_{1-42}$ monomers could pack into the shape depicted in panels C and D.

Table 1

Radii of gyration (Å), D_{max} (Å) and molecular mass (kDa) of $A\beta_{1-40}$:Cu^{2+} and $A\beta_{1-42}$: Cu^{2+} at sub and supra-equimolecular peptide/Cu ratios

Peptide	R_g Guinier	R_g GNOM	D_{max}	MM AUTOPOROD	MM MULCh
1.5 M/M $Cu^{2+}/A\beta_{1-40}$	39.7±1Å	43.5±2Å	123±2Å	47±3 kDa	51± 2kDa
0.5 M/M $Cu^{2+}/A\beta_{1-42}$	54.5±1Å	58.5±2Å	125±1Å	96±3 kDa	98±1kDa
1.5 M/M $Cu^{2+}/A\beta_{1-42}$	77±1Å	84±1Å	185±1Å	158±4 kDa	161±4kDa

Table 2

Relative distances between clusters obtained from DAMMIF

$A\beta_{1-40}$ 1.5M/MCu^{2+}		$A\beta_{1-42}$ 0.5 M/M Cu^{2+}		$A\beta_{1-42}$ 1.5 M/M Cu^{2+}	
Clusters	distances*	Clusters	distances*	Clusters	distances*
1 2	0.5050	1 2	0.5576	1 2	0.6924
1 3	0.5239	1 3	0.5944	1 3	0.6287
1 4	0.5124	1 4	0.5836	1 4	0.6251
1 5	0.5164	1 5	0.5684	1 5	0.7118
1 6	0.5296	1 6	0.6209	1 6	0.6385
1 7	0.5208	1 7	0.5861	1 7	0.6299
2 3	0.5401	2 3	0.6225	2 3	0.7599
2 4	0.5366	2 4	0.6030	2 4	0.6625
2 5	0.5231	2 5	0.5490	2 5	0.6742
2 6	0.5306	2 6	0.5506	2 6	0.5527
2 7	0.5336	2 7	0.5532	2 7	0.7793
3 4	0.5463	3 4	0.5925	3 4	0.7521
3 5	0.5397	3 5	0.6236	3 5	0.7730
3 6	0.5620	3 6	0.5660	3 6	0.6214
3 7	0.5508	3 7	0.6219	3 7	0.7242
4 5	0.5712	4 5	0.5968	4 5	0.6993
4 6	0.5467	4 6	0.6542	4 6	0.5897
6 7	0.5730	6 7	0.6235	6 7	0.7728
5 6	0.5543	5 6	0.5660	5 6	0.6722
5 7	0.5792	5 7	0.6036	5 7	0.6960

*Truncated from 13 places

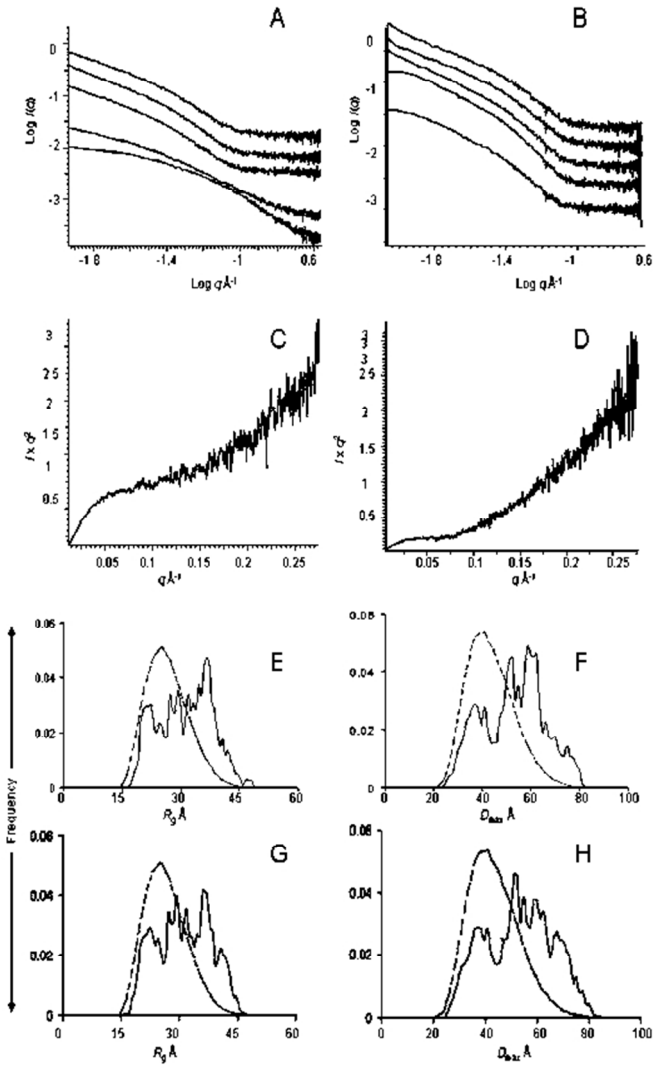

Figure 1: Scattering data from rapid mix experiments. A) Profiles of Aβ1-40 taken at 1.2 second intervals reading up from lowest curve after mixing from 15 mM KOH solution into 10 mM phosphate 150 mM NaCl pH 7.4 buffer. B) Profiles of Aβ1-42 taken after mixing, 1.2 sec. intervals between curves also reading up from lowest curve, C) Kratky plot calculated from the 1st 1.2 sec. Aβ1-40 profile. D) Kratky plot from the 1.2 sec. Aβ1-42 profile. E) Rg distribution calculated using Advanced EOM 2.0 from the 1.2 sec Aβ1-42 profile. F) EOM derived Dmax distribution for the 1.2 sec Aβ1-42 profile. G) EOM derived Rg distribution for the 1.2 sec Aβ1-40 profile. H) EOM derived Dmax distribution for the 1.2 sec Aβ1-40 profile. Dotted lines in panels E, F, G and H represent the pools of Rg and Dmax values generated from the peptide sequences. The solid lines represent the ensemble values.
190x254mm (96 x 96 DPI)

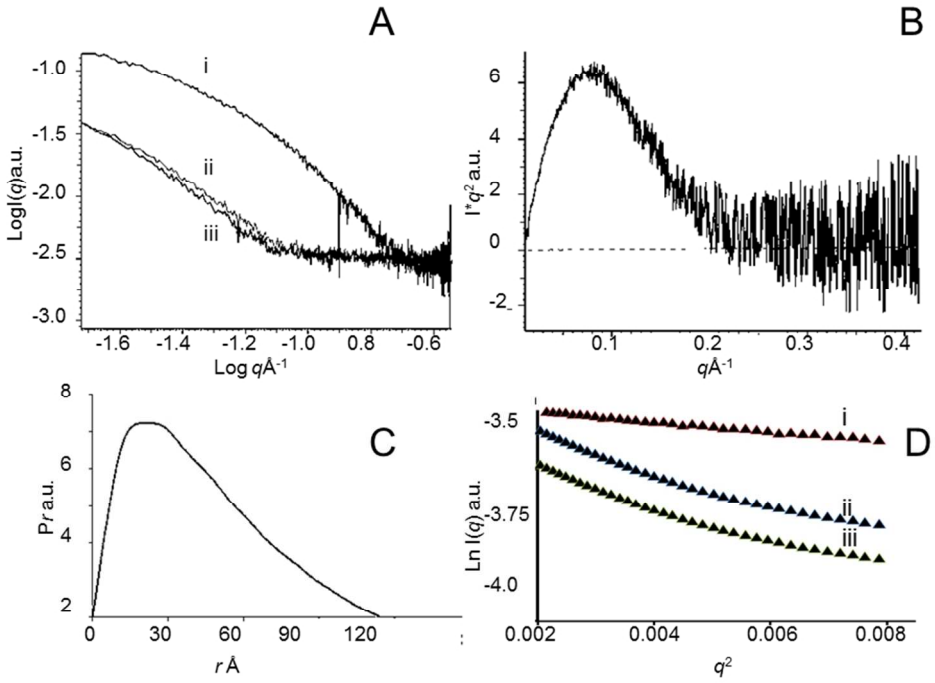

Figure 2: Scattering data for Cu2+/Aβ1-40 at sub and supra-equimolecular ratios.
A) Scattering profiles. Curve (i) Aβ1-40 in 1.5 M/M Cu2+, (ii) Aβ1-40 0.5 M/M Cu2+ B) Kratky plot of 1.5 M/M Cu2+/Aβ1-40 . C) Pair distribution analysis plot (P(r)) of 1.5 M/M Cu2+/Aβ1-40 . D) Guinier plots of (i) 1.5 M/M Cu2+/Aβ1-40 , (ii) 0.5M/M Cu2+/Aβ1-40 , and (iii) Aβ1-40 rapidly mixed from KOH to buffer.

254x190mm (96 x 96 DPI)

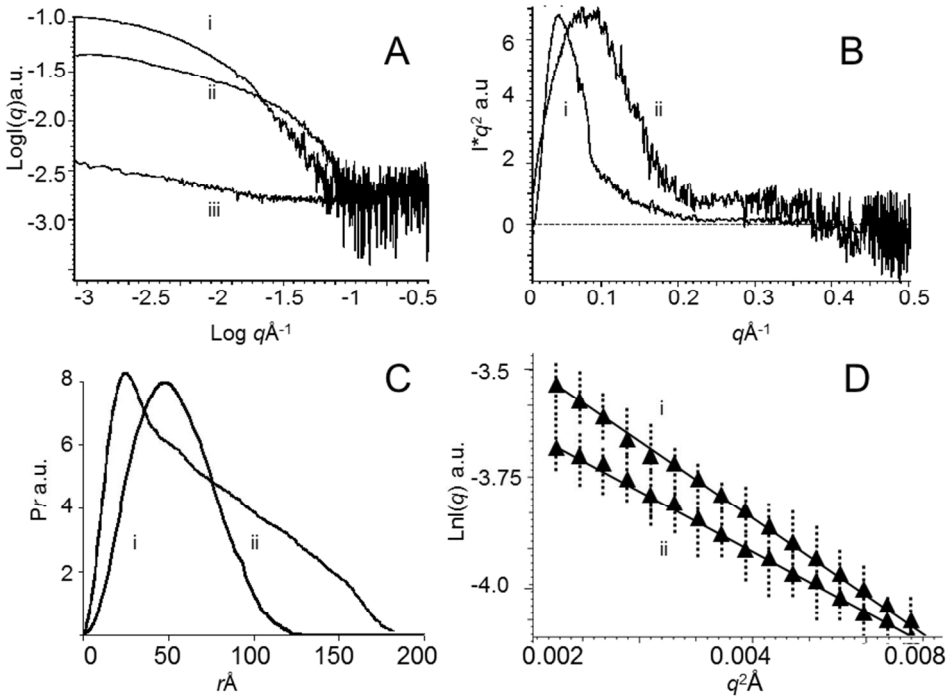

Figure 3: Scattering data for Cu2+/Aβ1-42 in sub and supra-equimolecular ratios. A) Scattering profiles for (i) Aβ1-42 in 1.5 M/M Cu2+, (ii) Aβ1-42 in 0.5 M/M Cu2+ and (iii) Aβ1-42 in buffer for comparison. B) Kratky plots of (i) 1.5 M/M Cu2+/Aβ1-42, (ii) 0.5 M/M Cu2+/Aβ1-42. C) Pair distribution analysis plot (P(r)) of (i) 1.5 M/M Cu2+/Aβ1-42, (ii) 0.5 M/M Cu2+/Aβ1-42. D) Guinier plot of (i) 1.5 M/M Cu2+/Aβ1-42, (ii) 0.5 M/M Cu2+/Aβ1-42
254x190mm (96 x 96 DPI)

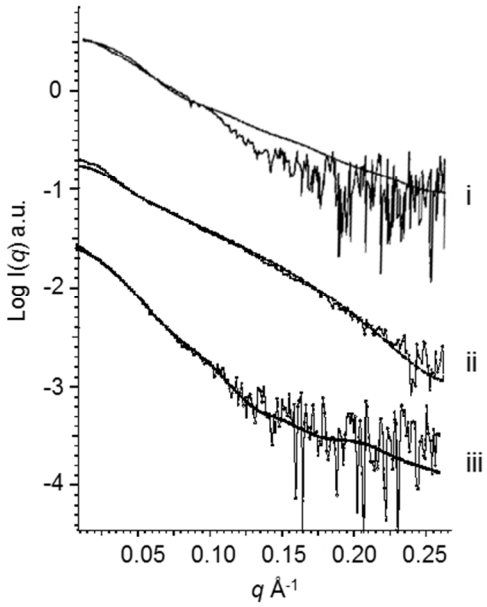

Figure 4: Fit of cylindrical and ellipsoidal bodies to scattering profiles; (i) Lack of fit of a cylinder to 1.5 M/M Cu2+/Aβ1-42 ; (ii) Fit of a cylinder to the profile of 0.5 M/M Cu2+/Aβ1-42; (iii) Fit of an ellipsoid of rotation to the profile of 1.5 M/M Cu2+/Aβ 1-42.
190x275mm (96 x 96 DPI)

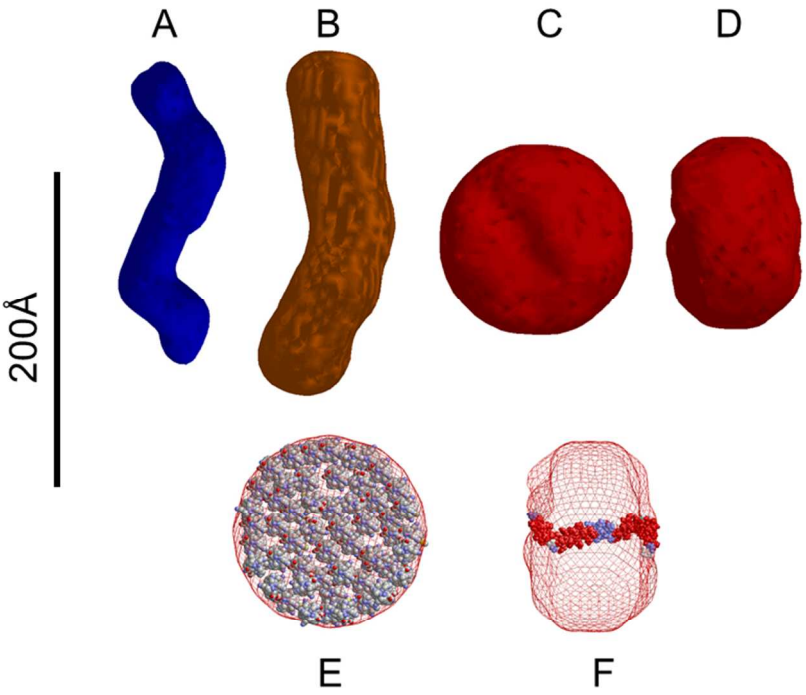

Figure 5: Cartoons of ab initio models produced by using DAMMIF of A. 1.5 M/M Cu2+/Aβ1-40 , B. 0.5 M/M Cu2+/Aβ1-42, C. 1.5 M/M Cu2+/Aβ1-42, D. side view of ellipsoid of rotation, E and F showing how Aβ1-42 monomers could pack into the shape depicted in panels C and D.
254x190mm (96 x 96 DPI)